MATERIALS SCIENCE

Shear-solvo defect annihilation of diblock copolymer thin films over a large area

Ye Chan Kim[1], Tae Joo Shin[2], Su-Mi Hur[3]*, Seok Joon Kwon[4]*, So Youn Kim[1]*

Achieving defect-free block copolymer (BCP) nanopatterns with a long-ranged orientation over a large area remains a persistent challenge, impeding the successful and widespread application of BCP self-assembly. Here, we demonstrate a new experimental strategy for defect annihilation while conserving structural order and enhancing uniformity of nanopatterns. Sequential shear alignment and solvent vapor annealing generate perfectly aligned nanopatterns with a low defect density over centimeter-scale areas, outperforming previous single or sequential combinations of annealing. The enhanced order quality and pattern uniformity were characterized in unprecedented detail via scattering analysis and incorporating new mathematical indices using elaborate image processing algorithms. In addition, using an advanced sampling method combined with a coarse-grained molecular simulation, we found that domain swelling is the driving force for enhanced defect annihilation. The superior quality of large-scale nanopatterns was further confirmed with diffraction and optical properties after metallized patterns, suggesting strong potential for application in optoelectrical devices.

INTRODUCTION

The self-assembly of block copolymer (BCP) thin films has been extensively exploited on the basis of their potential for use in several industrial applications requiring periodic nanostructures (*1*–*4*). The ability to create dense periodic structures over large areas, with 10- to 100-nm features has been of particular interest, and is expected to cost-effectively overcome technical limitations associated with conventional lithographic techniques (*5*). While the self-assembly of BCP thin films provides fine resolutions, versatility and scalability fulfilling the criteria for nanopatterns, controlling the shape orientation for long-range order, and minimizing the density of large-area defects are still far from satisfactory.

Directed self-assembly (DSA) including graphoepitaxy (*6*, *7*), surface chemical patterning (*8*, *9*), and laser-assisted patterning (*10*, *11*) have achieved significant milestones in enhancing the controllability of structural orientation and ordering of the nanoscale structures of BCPs. On the basis of the processing perspective, however, DSA typically requires multistep approaches in locating and aligning nanopatterns followed by long-range orders, which are particularly expensive. Furthermore, despite the use of external fields in DSA (*12*, *13*), reducing defect density in the nanopatterns for practical application [i.e., <1 ea (each)/cm^2] has yet to be experimentally demonstrated (*14*).

Defects observed in BCP thin films include disclinations, dislocations, and shape roughness, which are topologically equivalent to those occurring in typical crystalline materials. However, compared with conventional inorganic materials, the mechanisms underlying the origin of defects and defect annihilation in BCPs have yet to be completely elucidated. Only recently, defects were found to be kinetically trapped structures occurring in the course of the initial ordering process (*15*–*18*). In particular, higher segregation strength, χ, between the blocks is believed to enhance the thermodynamic driving force ordering the self-assembly patterns, which also corresponds to the increase in the kinetic energy barrier interfering with defect annihilation (*15*). In addition, in the case of the most advanced chemoepitaxy-assisted DSA in terms of long-range ordering and defect control, the guiding stripes were found to yield an additional energy barrier (*19*). These studies suggest that thermodynamically optimized DSA is not necessarily in accordance with kinetically optimized defect annihilation.

Alternative experimental strategies were used to reduce defect density. DSA associated with classical annealing methods such as thermal annealing, solvent vapor annealing (SVA), or their combination have further reduced the defect density of BCP nanopatterns in a large area. In particular, a photothermal process introduced by Jin *et al.* (*20*) showed ultrafast self-assembly of BCPs with a low level of defect conserving a long-range order. In addition, Majewski and Yager (*21*) suggested an effective kinetic pathway starting from a latent state for alignments with low defect density. Recently, Kim *et al.* (*22*) reported that blending short random copolymers in the BCPs notably reduces the defect density by increasing chain mobility and, thus, creating nanopatterns with larger grain size. However, these attempts are not effective in reinforcing orientational uniformity over large areas. In other words, the current level of BCP nanopatterning lags substantially behind the simultaneous well-aligned orientation unnecessary expression macroscopically and annihilation of defects microscopically.

In this study, we demonstrate a new experimental method of annealing defects and sustaining the orientational order and enhancing pattern uniformity of the self-assembled BCP thin film over centimeter-scale areas. In this method, we used a divide-and-conquer strategy based on mechanical shear-assisted orientation followed by SVA-driven defect annihilation [namely, shear-solvo (SS) annealing], as illustrated in Fig. 1. Since the study of BCP thin films by Angelescu *et al.* (*23*), mechanical shearing or its adaptation in other forms such as laser and polydimethylsiloxane (PDMS) (*24*–*29*) have been frequently used to generate nanopatterns with a controlled orientation based on its accessibility and scalability. While shear alone often yielded substantially low defect density and high quality of alignment (*30*, *31*), the defect density and quality of alignment can vary from polymer to polymer. Unfortunately, shearing can still be associated with the development of inherent defects.

Thus, we suggest independent control of the orientational order and annihilation of the defects via stepwise shearing and SVA. First, shearing

[1]School of Energy and Chemical Engineering, Ulsan National Institute of Science and Technology (UNIST), Ulsan 44919, Republic of Korea. [2]UNIST Central Research Facilities and School of Natural Science, UNIST, Ulsan 44919, Republic of Korea. [3]School of Polymer Science and Engineering, Chonnam National University, Gwangju 61186, Republic of Korea. [4]Nanophotonics Research Center, Korea Institute of Science and Technology, Seongbuk-Gu, Seoul 02792, Republic of Korea.
*Corresponding author. Email: shur@chonnam.ac.kr (S.-M.H.); cheme@kist.re.kr (S.J.K.); soyounkim@unist.ac.kr (S.Y.K.)

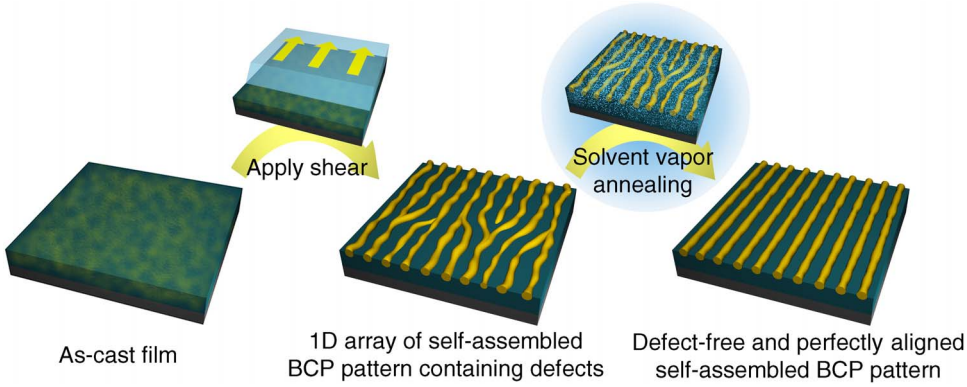

Fig. 1. Schematic illustration of the SS annealing process of BCP thin films. 1D, one-dimensional.

induces macroscopic orientational order. Next, the solvent annealing annihilates microscopic defects in the aligned patterns without interfering with shear-induced long-range orientation. To demonstrate the performance of the SS annealing in achieving greatly aligned BCP nanopatterns with long-range orientational order and substantially reduced defect density, we optimized the experimental conditions. The performance was analyzed with unprecedented detail thanks to newly devised numerical methods and algorithms, as well as high-resolution scattering and imaging methods. We also elucidated the fundamental mechanisms underlying defect annihilation using coarse-grained molecular simulations. Last, we established the pattern quality and demonstrated the practical applicability of the resulting nearly perfect BCP nanopatterns via construction of a parallel array of metallic nanowires over a centimeter-scale area.

RESULTS

SS annealing procedure

Defect annihilation with SS annealing was systematically investigated using cylinder-forming polystyrene-*b*-poly(2-vinylpyridine) (PS-*b*-P2VP), which has a number-average molecular weight of 44-*b*-18.5 kg/mol (Fig. 1) (*32*, *33*). To ensure self-assembly, we carefully controlled the film thickness around 38 nm, which is close to the *d*-spacing (L_0 ~ 40 nm) and the optimal thickness, resulting in adequate alignment quality, as previously reported (*32*). Shearing conditions such as shearing stress (20 kPa) and temperature (160° to 170°C) were determined to ensure sufficient mobility of polymer chains with the best alignment. After shearing, we exposed the thin films to vapors of various solvents [i.e., toluene, tetrahydrofuran (THF), and their mixture with a 7:3 volumetric mixing ratio] in a closely sealed chamber for desirable annealing time.

Structural order control

Figure 2 shows the structural change in BCP thin films after shear only followed by SS annealing 15 min later. The mechanical shearing intrinsically directs the alignment of the cylinders along the shearing direction, as shown in Fig. 2. However, as shown in Fig. 2A, mechanical shearing is not sufficient to reduce the defects in the self-assembled patterns. By contrast, subsequent SVA under optimized conditions substantially enhances the orientational order and extends its persistence range, as shown in Fig. 2 (B to D). As provided in the scanning electron microscopy (SEM) images in the top row of Fig. 2 (A to D), SVA strongly increases the orientational order while preserving the initial shearing direction (SEM images for shorter SS annealing times are presented in fig. S1). Notably, to maintain the initial orientation after SVA, a sufficient level of ordering is required before SVA. For instance, as shown in fig. S2, when shear is applied at relatively low temperatures (i.e., <160°C), the initial orientational order disappears during the course of the SVA procedure. This phenomenon is attributed mainly to the existence of high defect density induced by low chain mobility, which indicates that shearing under nonoptimized conditions leads to the BCP films to terrace during the SVA.

On the basis of the two-dimensional (2D) grazing incidence small-angle x-ray scattering (GISAXS) maps depicted in the bottom row of Fig. 2 (B to D), we also confirm that the orientational order was enhanced by SS annealing over a large area. The corresponding GISAXS maps with SS annealing at shorter times are also provided in fig. S1. In particular, the maps show sharp peaks and appearance of higher-order peaks in the SVA-applied films (Fig. 2, B to D) when compared with the shear-only film (Fig. 2A). GISAXS data also indicate that SVA notably reinforces the structural order of a self-assembled BCP pattern. For instance, as shown by the scattering intensities as a function of the wavenumber (q) in Fig. 2E, we noticed that the peak broadening is diminished in the SVA-applied BCP thin films compared with the shear-only films.

Typically, the peak broadening in a small-angle scattering is induced by an increase in the nonuniform microstrain and thermal disorders, which lead to fluctuations in the characteristic spatial length scales such as *d*-spacing (L_0) and/or width of the cylinders (*34*). We numerically calculated the broadening behavior of the primary scattering peak (i.e., the first-order peak at $q = 2\pi/L_0$) quantified by the full-width at half maximum or integral breadth as a function of the domain spacing uncertainty. On the basis of the analysis, we confirmed that the peak broadening increases in intensity with the increased fluctuations of domain spacing (see the Supplementary Materials). As shown in Fig. 2F, the integral breadth decreases with increasing SVA duration up to 15 min irrespective of the solvent. In particular, the peak width is significantly reduced from 2.33×10^{-3} Å^{-1} in the shear-only case to 7.70×10^{-4} Å^{-1} in the case of SS with solvent mixture or to 8.70×10^{-4} Å^{-1} in the case of SS with THF. The reduced peak width ratio (i.e., a factor of 2.68 to 3.03) is in accordance with the theoretical calculation (see the Supplementary Materials) involving cases showing a fluctuation of 2% versus 10% in periodicity (with a factor of 2.6 for the peak width ratio). Assuming a 10% periodicity fluctuation in the case of shear-only films (reference sample), we can estimate the relative enhancement factor of the domain

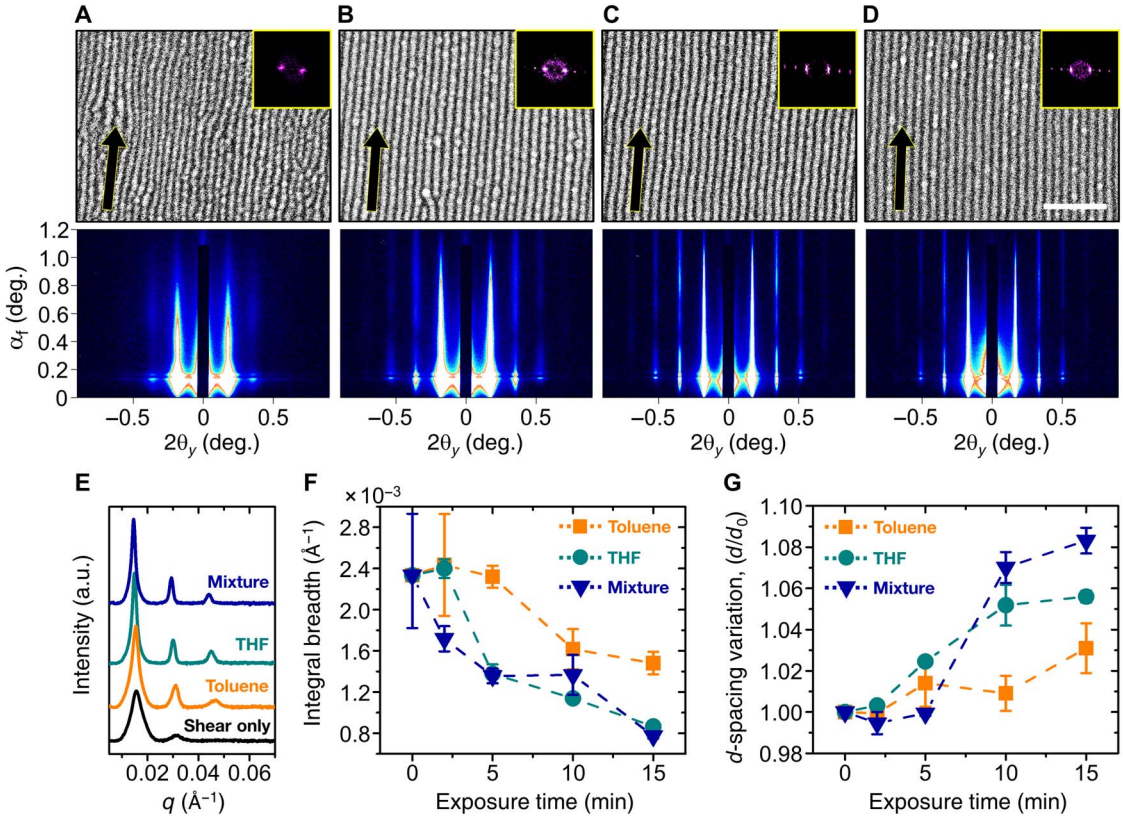

Fig. 2. Long-range structural order control of SS-annealed cylinder patterns. SEM and grazing incidence small-angle x-ray scattering (GISAXS) 2D images after (**A**) shear-only and SS annealing with (**B**) toluene, (**C**) THF, and (**D**) their mixture for 15 min. The insets show fast Fourier transform (FFT) patterns obtained from each SEM images, and the arrows indicate the orientation direction, which is determined from the azimuthal angle distribution of each FFT image. (**E**) GISAXS 1D profiles, (**F**) integral breadth of first-order peaks, and (**G**) normalized *d*-spacing variation with that of shear-only films were obtained from GISAXS 2D data. 1D profiles were vertically shifted for clarity, and each error bar represents the range from average value. Scale bar in SEM image in (D), 300 nm. All SEM images have the same magnification. a.u., arbitrary units.

spacing uniformity for the SS-treated cases such as 3.0 for toluene, 5.0 for THF, and 5.8 for mixture.

Another notable finding is the increasing lateral *d*-spacing with increased duration of SVA. As shown in Fig. 2G, we observed that *d*-spacing (or periodicity) increased by 3 to 8% when the self-assembled BCP pattern was exposed to solvents. The variation in *d*-spacing depends on the solvent type. The penetration of solvent molecules into the polymer chains leads to swelling of the film, which results in increased film thickness and larger lateral *d*-spacing (*35*, *36*). The swelling is more effective for a good solvent; therefore, the increase in *d*-spacing is more pronounced. The increased *d*-spacing substantially contributes to the relaxation of defects in the self-assembled patterns. During the SVA-induced relaxation, the conformation of chains in the sheared film approaches the thermodynamic equilibrium, which also provides a kinetically favored pathway for defect melting. We will discuss the detailed mechanism underlying the SVA-induced defect annihilation in terms of dynamics of *d*-spacing.

Quantitative analysis of defects and pattern uniformity

To precisely validate the defect annihilation performance of SS annealing, we calculated a few quantitative indices to elucidate the structural order and uniformity of the self-assembly patterns. On the basis of the SEM images of the self-assembled BCPs [first column of Fig. 3A (shear-only), Fig. 3B (SS with toluene), Fig. 3C (SS with THF), and Fig. 3D (SS with mixture)], we first calculated the orientational order of the patterns. Numerical analysis of the orientation vector maps [i.e., 2D maps in the second column of Fig. 3 (A to D) for the local orientation vectors depicted by an angular deviation from the average orientation angle of the pixels in the image] of the self-assembly patterns strongly indicates that the orientation of the cylinder-array patterns becomes uniform upon application of SVA with THF or solvent mixtures. The orientational uniformity can be quantified by calculating Hermans orientational parameter, P_2 (see the Supplementary Materials for the detailed formula). As indicated in Fig. 3E, the SVA using THF or solvent mixture notably enhances the orientational order of the cylinder-array pattern generating a nearly perfect alignment (i.e., $P_2 = 0.995$ compared to $P_2 = 1$ of an ideal 1D pattern). The greatly enhanced orientation can also be cross-validated via observations of increased orientational persistence length, L_p (see the Supplementary Materials), from $L_p = 3.83$ μm for the shear-only case to $L_p = 8.21$ μm for the case with SS using solvent mixture (see the inset of Fig. 3E). In addition, we determined this consistency by calculating the orientational order correlation length, L_c (see the Supplementary Materials). The pair correlation function $g(r)$ displayed in Fig. 3F decays more slowly in SS annealing with THF or solvent mixture compared with the reference (i.e., shear only), indicating that L_c is significantly extended by SS annealing. L_c is approximately doubled under SS annealing with solvent mixture (i.e., $L_c = 343.2$ nm versus $L_c = 172.7$ nm), as shown in the inset of Fig. 3F.

In addition to the analysis of orientational order, we developed previously unidentified numerical algorithms to quantitatively analyze

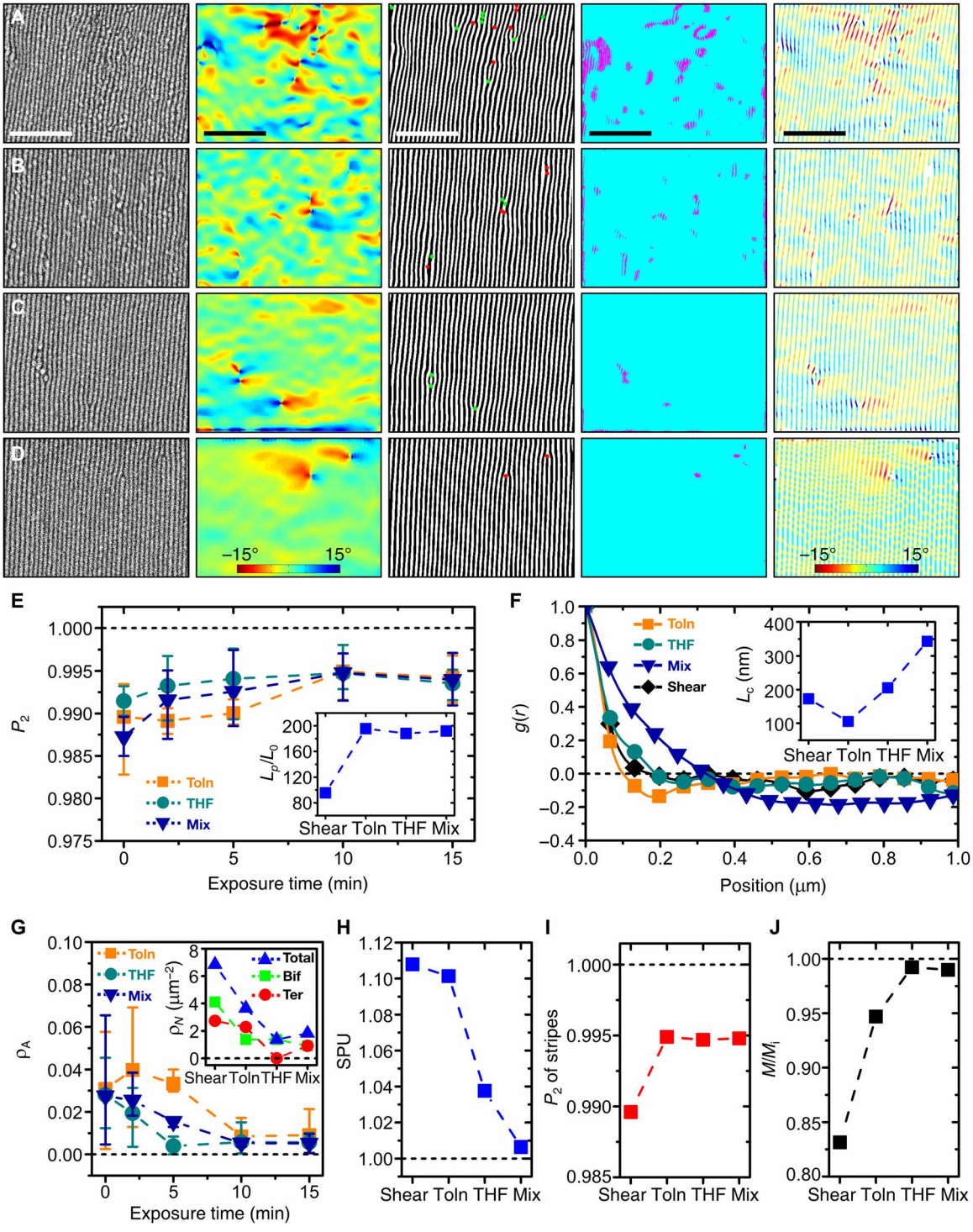

Fig. 3. Microscopic structural order analysis of SS-annealed cylinder patterns. The representative analysis results (SEM image, colored orientation of pixels, marked defect number, marked defect area, and colored orientation of stripes) of (**A**) shear-only, SS annealing with (**B**) toluene (Toln), (**C**) THF, and (**D**) their mixture (Mix) for 10 min are shown in each row from left to right. (**E**) Plot of Hermans parameter, P_2. The inset shows the scaled persistence length (L_p/L_0). (**F**) Plot of correlation function, $g(r)$. The inset shows the correlation length, L_c. (**G**) Plot of areal defect density, ρ_A. The inset shows the defect number density, ρ_N. Bif, bifurcation; Ter, termination. (**H**) Plot of stripe pattern uniformity (SPU). (**I**) Plot of P_2 of stripes. (**J**) Plot of scaled degree of matching with ideal patterns using Gabor filter. Each error bar represents the range from average value. Scale bars in (A), 500 nm.

topological defects (see the Supplementary Materials) and identify them along with the calculation of their number (the third column) and areal density [the fourth column of Fig. 3 (A to D)]. Using advanced image processing–based numerical algorithms, we counted two types of defects (i.e., bifurcation and termination) in the SEM images of self-assembled BCP patterns, which facilitated the calculation of the density of defects (ρ_N), as shown in the inset of Fig. 3G. As shown in the figure, SS with THF or solvent mixture yielded minimal defects and related number densities (i.e., 1.37 ea/μm^2 for THF and 1.83 ea/μm^2 for solvent mixture, respectively). We also used a newly developed algorithm to distinguish the areas affected by the defects [i.e., pinkish regions in the fourth column of Fig. 3 (A to D)] and calculated the areal density of defects (ρ_A), which is equal to the fraction of the defective area relative to the total area of the image. Notably, as shown in Fig. 3G, we found that ρ_A approaches an exceptionally low level such as $\rho_A \sim 5.20 \times 10^{-3}$ for self-assembled BCP patterns processed with SS using the solvent mixtures for the desired duration (i.e., 10 min).

Next, we also developed an additional index measuring the pattern quality, named stripe pattern uniformity (SPU), to confirm the overall performance of the SS annealing sustaining the orientational order and facilitating defect annihilation. Basically, SPU can be used to quantitatively measure the similarity between a given line-and-space–like pattern (i.e., stripe pattern) and the perfectly aligned and ordered pattern accompanied by equivalent domain spacing and orientational angle. Theoretically, SPU is equal to unity for the perfect line-and-space pattern. Using a simple arc length measuring algorithm (see the Supplementary Materials), we calculated the SPU of the self-assembly patterns of the images using selectively analyzed local orientation vectors of skeletonized stripes [the fifth column of Fig. 3 (A to D)]. As shown in Fig. 3H, SPU is practically unity in the case of SS annealing with solvent mixture (i.e., SPU = 1.006). Compared with P_2, SPU facilitates a clear and quantitative analysis of the degree of similarity of a given pattern relative to the ideal pattern, while P_2 is not effective in identifying the similarity (see the saturating behavior of P_2 for cases of SS with toluene, THF, and mixtures in Fig. 3I). To determine the advantages of SPU independently, we also measured the quality of the 1D pattern using a Gabor filter, which has been conventionally and frequently used to detect the intrinsic orientational angle and spatial periodicity of a given pattern (see the Supplementary Materials). By comparing the filtered magnitude of the given pattern, it enabled measurement of the quality of a line-and-space pattern. Theoretically, the normalized filtered magnitude is equal to unity for a perfect line-and-space pattern. As shown in Fig. 3J, the normalized magnitude approaches unity in the cases of SS with THF and mixture (i.e., 0.992 for THF and 0.990 for mixture, respectively). These results indicate that the Gabor filter–based algorithm is not effective in discriminating the two cases compared with SPU.

As a complementary approach, we also analyzed the line edge roughness (LER) and the line width roughness (LWR) using an image processing algorithm (see the Supplementary Materials). We found that both LER and LWR were effectively reduced by the SS method in conjunction with THF and solvent mixtures [i.e., LER of 4.7 nm and LWR of 7.0 nm annealed for 10 min; see fig. S11 (C and D)]. The reduction in LER and LWR is in accordance with the enhanced orientational order and pattern uniformity. Further reduction in LER/LWR can be achieved via appropriate etching and pattern transfer (*37*). On the basis of the detailed analysis of defects and pattern uniformity of the self-assembled BCP pattern, we conclude that the SS annealing with solvent mixture and/or THF is the most advanced strategy to sustain the orientational order and enhance defect-free uniformity of self-assembled BCP nanopatterns.

Solvent preferences and long-time effect

As illustrated in Figs. 1 and 2, it is important to select the appropriate solvent and exposure time during the SS. Thus, we analyzed the solvent preferences by monitoring the thickness variation of swollen films of PS-*b*-P2VP, PS, and P2VP with SVA (see the Supplementary Materials). Upon SVA, the thickness of the shear-aligned PS-*b*-P2VP film, P2VP homopolymer film, and PS homopolymer film increases much faster with THF than with toluene. While THF is a good solvent both for P2VP and PS blocks, toluene is preferred for the PS block than the P2VP block (*38*). Furthermore, the vapor pressure of THF is higher than that of toluene. Thus, the swelling ratio of the blocks also suggested that SVA with THF is more appropriate in ensuring a balanced swelling of the two blocks at later stages (fig. S12). By contrast, SVA with toluene showed reduced balanced swelling between blocks, which results in thinner cylinder domains, and even order-to-disorder transition at longer intervals of time (*39*). Therefore, it is rational to use THF for the SVA over toluene.

It is also important to control the annealing time during the course of the SS. Prolonged swelling in the presence of a good solvent resulted in restructured film. As shown in fig. S13 (A and B), sufficiently prolonged exposure to THF vapor (i.e., 60 min) induced dewetting of the BCP film and/or terracing in the film. Penetration of the solvent molecules into the thin films leads to swelling; thus, the increased thickness with swelling is not at an equilibrium thickness, resulting in terracing of films. Film terracing requires migration or depletion of polymer chains to form double layers or a monolayer. Note that the BCPs in the double-layer zone still maintain the initially sheared orientation, whereas the BCPs in the monolayer zone show random orientation. The newly formed cylinders in the top layer of the double-layer zone are locally oriented along the shearing direction of the bottom layer, while depletion of the chains in the monolayer zone allows BCPs to lose the initial orientation.

Upon exposure to the mixture vapor, the macroscopic structures were stable without any notable morphological changes even after 60 min of SVA (fig. S13C). In addition, we also observed that prolonged exposure did not deteriorate the orientational order or defect densities (see table S2). On the basis of the perspective of swelling kinetics, the mixed solvent vapor slows swelling compared with exposure to THF alone. While the rapid increase in film thickness with THF vapor induces terracing (fig. S13, A and B), the retarded swelling with the mixed solvent vapor prevents the terracing or dewetting of the films. Combination with a high–boiling point solvent may increase the time ensuring defect annihilation and slowly increase the film thickness. Therefore, on the basis of the comparative performance of sustained orientational order, defect annihilation, and enhanced pattern uniformity provided by SS with THF and solvent mixture, it is appropriate to use the solvent mixture for SVA rather than THF for the realization of morphologically stable thin films with pattern uniformity. We further note that the SVA process certainly increases orientation order and decreases defect density; however, the results can be sensitive to changes in SVA setups such as drying rate, chamber size, and vapor injection method.

Minimum free energy path for defect annihilation

The equilibrium self-assembly of BCP is driven by thermodynamic forces; thus, ordering may be enhanced by magnifying the free energy difference between defective and ordered states (defect formation energy) using external fields such as shear. However, for microscopic defects, recent studies suggest that the defect annihilation, particularly at the later stage of self-assembly of BCP films, is an activated process that

can be accelerated by lowering the kinetic energy barriers. In other words, for defect annealing, it is not always advantageous to use conventional strategies of increasing defect formation free energy (i.e., high χ BCP) because it increases the kinetic energy barrier (*15*, *16*). As suggested by our recent study, guiding strips used in DSA could alter the kinetic path of defect annihilation and stabilize the defects by kinetically trapping them (*19*). Thus, the proposed annihilation mechanism of SS annealing needs to be appreciated in the context of free energy paths focused on the variation of kinetic energy barriers.

During SVA, the system is at a nonequilibrium state, as solvent molecules continuously flow into the film, which naturally promotes chain migration for defect annihilation. This increased chain mobility and lowered segregation strength between the blocks are well-known advantages of the SVA process; however, it may not solely explain the higher performance of SS annealing. Chain mobility can be readily enhanced with THF, toluene, or mixed solvent vapors, although the defect annihilation with toluene was not as efficient compared with THF or mixed vapor.

The lateral *d*-spacing of shear-aligned film increased under continued SVA, as shown in Fig. 2G. In addition, we found that the shear alignment provides directional guidance of ordering, although the *d*-spacing of the shear-aligned film was reduced from the optimal value of bulk state. As shown in fig. S14, the *d*-spacing of shear-aligned BCP thin films in this study was smaller than that of the thermally annealed thin films at equilibrium thicknesses. We found that shrunken *d*-spacing during the shear-alignment was restored eventually to the equilibrium value as SVA progressed, suggesting that the shear-compressed chains were relaxed by SVA to ensure optimal *d*-spacing. The simultaneous reduction in the number of defects with the increase in *d*-spacing suggests that the changes in chain conformation may effectively modulate the kinetic pathways of defect annihilation and thus represent an intrinsic driving force for enhanced defect annihilation.

Takahashi *et al.* (*17*) calculated the defect formation energy of three lamellar periods with BCPs in a channel under compressive and tensile strains. They showed that the defect formation energy was reduced upon application of a tensile or compressive strain. Since kinetic energy barrier rather than defect formation energy is crucial for defect annihilation, we investigated the effect of *d*-spacing on the kinetics of defect annihilation by calculating the minimum free energy pathways (MFEPs) of defect annihilation in a symmetric BCP thin film at χN = 20, using the string method combined with theoretically informed coarse-grained (TICG) simulations.

We conducted the MFEP estimation under various periodicities of L (*d*-spacing) including 1.655, 1.728, 1.8, 1.9, 2.0, and 2.1 R_e, where R_e denotes the end-to-end distance; the simulation box size in the lateral direction was selected as multiples of periodicity L (*d*-spacing) ($L_x = 6L$), while L_y and L_z were fixed at 8.275 and 1.655 R_e, respectively. A defective structure carrying a dislocation pair with opposite Burger vectors was selected as an initial state, while the final morphology corresponded to a perfectly ordered state. Predicted morphology and free energy changes in k_BT along the reaction coordinate α, which varies from 0 to 1, under compressive and tensile strains are shown in Fig. 4A. Insets display the morphologies of the initial defective (α = 0), transition, and final defect-free states (α = 1).

In Fig. 4B, the defect formation energy, ΔF_d (free energy difference between states at α = 0 and α = 1, blue), and kinetic energy barrier, ΔF_b (free energy difference between states at α = 0 and the transition state, black), expressed in units of k_BT, are plotted as a function of periodicity of lamellae. We calculated ΔF_d and ΔF_b by averaging over 10 finally converged MFEPs, and each error bar represents the SD.

ΔF_d is concave as a function of periodicity, with a maximum at L/R_e = 1.9, indicating the thermodynamically optimal *d*-spacing of the system. Simultaneous compression (L/R_e < 1.9) or extension (L/R_e > 1.9) of *d*-spacing results in an increase of ΔF_b and a decrease of ΔF_d, compared with that of ΔF_d, and ΔF_b monotonically changes as a function of χN (*15*). Note that the increase in ΔF_b is unexpectedly large with a magnitude of 5.1 k_BT when the chain is compressed by 13% to $L = 1.655R_e$ from the optimal periodicity of $L = 1.9R_e$. The shear compressed *d*-spacing and the spacing was increased by about 10% with SVA, as shown in Fig. 2G.

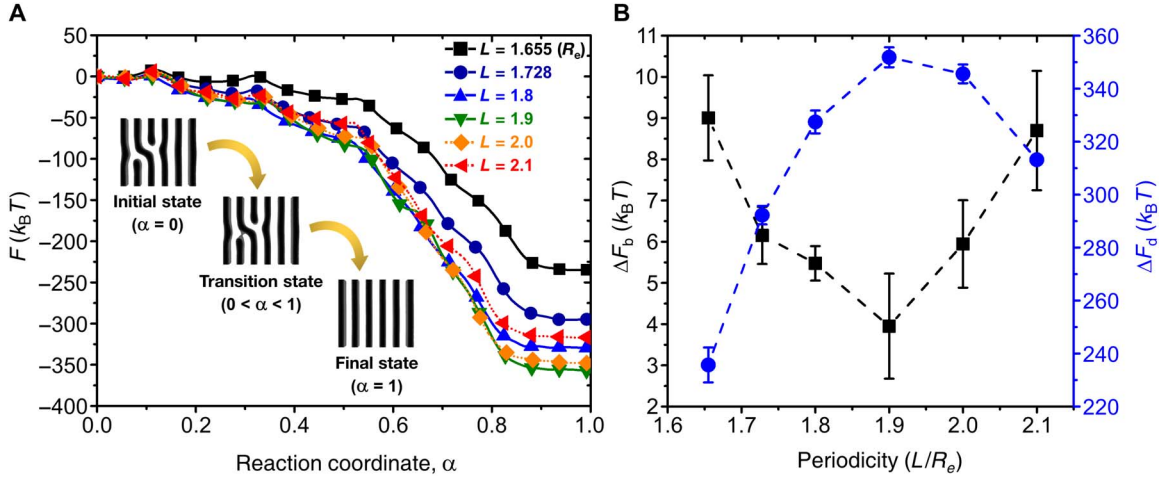

Fig. 4. MFEP calculation. (**A**) MFEPs between defective (dislocation dipole) and defect-free lamellar structures in symmetric BCP thin film at χN = 20. The *x* axis represents the reaction coordinate α along the pathway, while the *y* axis shows the free energy difference from the starting defective morphology, in units of k_BT. Morphologies of the initial defective (α = 0), transition, and final defect-free (α = 1) states are shown in insets. Periodicity, *L*, of lamellae varies from 1.655, 1.728, 1.8, 1.9, 2.0, to 2.1 R_e (end to end distance of polymer chain). The system size in lateral direction varies accordingly to $L_x = 6L$, while L_y and L_z are fixed at 8.275 and 1.655 R_e, respectively. (**B**) Defect formation energy, ΔF_d (free energy difference between states at α = 0 and α = 1, blue), and kinetic energy barrier, ΔF_b (free energy difference between states at α = 0 and the transition state, black), in units of k_BT, as a function of periodicity of lamellae. Each error bar shows the range from the average values.

Since the defect annihilation time is proportional to exp($-\Delta F_b$), variation in ΔF_b by more than 55% (2.2 k_BT) will result in significant changes in defect removal kinetics. This phenomenon explains why shearing alone or shearing followed by thermal annealing (discussed later) is not efficient for defect removal, which requires a compressed state with a large energy barrier, ΔF_b. On the other hand, SVA after shearing not only increases chain mobility and reduces the effective χN but also restores the optimal *d*-spacing and, hence, significantly reduces the kinetic energy barrier for defect annihilation. The simultaneous increment of *d*-spacing with SVA suggests that the domain swelling and the released chain compression represent an intrinsic driving force for defect annihilation and increased chain mobility. Further increase in *d*-spacing with prolonged SVA is undesirable as it increases the ΔF_b again, leading to terracing of the film without increasing the *d*-spacing.

Comparison with other annealing methods

To validate the authenticity of the present SS annealing, we compared SS-treated BCP thin films with shear-thermal–annealed (namely, ST annealing) BCP thin films in terms of structural order of the self-assembled patterns (at 150°C up to 60 min). As shown in fig. S15, the ST-annealed BCP films exhibited worse structural order [i.e., broader primary scattering peak in 2D GISAXS in fig. S15 (A, C, and D)]. The ST-annealed film even showed dewetting and terracing only after 15 min of annealing (fig. S15B) despite moderate annealing conditions. The morphological instability may be attributed to the thickness, which was not at equilibrium. Furthermore, we observed that *d*-spacing increased only by 1 to 2% with thermal annealing for 60 min. The nonequilibrium *d*-spacing also lowered the possibility of defect annihilation. The limited ability of ST annealing for defect annihilation and small variation in *d*-spacing with ST annealing indicate severe changes in chain conformation and mobility with SS than with ST annealing. The ST annealing at a monolayer thickness of 58 nm (250°C up to 15 hours) was also performed (fig. S15, F to H). We observed order enhancement and reduced defect density; however, the films showed poor uniformity over a large area and required a long time to remove defects while losing the order.

We also compared possible combinations of other known annealing methods. As shown in fig. S16, every possible combination of the conventional annealing methods [i.e., thermal annealing (A), solvo annealing (B), thermal-solvo annealing (C), and solvo-thermal annealing (D)] without initial application of the shear did not yield well-aligned long-range orientational order of cylinders over the long range. When thermal or solvo annealing was performed before shear [i.e., thermal-shear (E) and solvo-shear (F)], cylinders were aligned along the shear direction exhibiting long-range orientational order, as shown in fig. S16E and fig. S16F, respectively. However, both exhibited a great deal of defects and non-smooth line edge profiles. This comparison suggests that the implementation of the initial orientational order provided by shearing followed by defect annihilation induced by SVA is a unique approach to generate well-aligned and defect-free self-assembled BCP nanopatterns over a large area.

Global pattern uniformity over large areas

While the proposed SS annealing can be effective over a large area (i.e., >1 cm^2), the quantitative analysis of SEM images and GISAXS data only provides local information because of the limitations of high-magnification SEM (i.e., <10 μm) and typical beam size of the GISAXS (i.e., <1 mm). Thus, we investigated the global consistency of pattern uniformity. As shown in Fig. 5A, we obtained SEM images of nine regions in shear-only and SS-annealed samples with an area of 1.2 cm by 1.2 cm. As apparent from the representative SEM images of each position (fig. S17), SS annealing was effective and consistent over centimeter-scale areas. A detailed analysis of the ordering quality at each position was performed using the parameters introduced in Fig. 3: the orientation parameter (Fig. 5B), areal defect density (Fig. 5C), SPU (Fig. 5D), and normalized Gabor-filtered magnitude (Fig. 5E). Notably, in addition to improvement of all parameters by SS annealing compared with the shear only, position-dependent variation of each parameter was also significantly reduced. These results reaffirm the effectiveness of SS annealing for achieving BCP self-assembly nanopatterns with a well-aligned orientational order and low defect density over a centimeter-scale area, which has potential applications ranging from BCP nanolithography and industrial applications.

To confirm the enhanced performance and test the industrial applications of the suggested annealing method, we transformed the BCP self-assembly nanopatterns into metallic nanowire arrays. The sub–100-nm periodic and uniform metallic nanostructures represent promising application as nanoscale integrated circuits (*40*), data-storage media (*41*), catalysts (*42*), and even optoelectronic devices such as substrates for surface-enhanced Raman spectroscopy (*43*) and plasmonic platforms (*44*). In the light of these applications, the SS-annealed BCP self-assembly nanopatterns were converted into an array of metallic nanowires by incorporating metal ions followed by selective O_2 reactive ion etching (*45*). As shown in Fig. 5F, the conversion successfully generated a well-aligned 1D array of gold nanowires (periodicity, ~40 nm; width, ~15 nm; height, ~20 nm) over a centimeter-scale area. The generation of patterns over an entire wafer may benefit from the proper modification of shearing techniques (*24*–*29*).

We measured the diffraction intensity of the 1D array of gold nanowires using x-ray double crystal Bragg diffraction (XRBD). The ideal nanoscale 1D grating structures with relevant contrast of the dielectric constant along the grating vector are expected to display a series of diffraction peaks in the diffraction rocking curve. The peaks are responsible for the multislit Fraunhofer diffraction patterns (*46*). As shown in Fig. 5G, it is evident that the quality-controlled 1D self-assembly pattern obtained from the optimized SS annealing facilitates construction of an exceptionally uniform 1D array of gold nanowires. This finding is significant when compared with the diffraction rocking curves of 1D metallic nanostructures constructed from 1D self-assembly patterns generated by the shear-only process.

We also measured the spectral behaviors of the 1D metallic nanostructures under polarized ultraviolet–visible–near-infrared (UV-Vis-NIR) light. We measured the difference of the spectral reflectance from the sample between transverse electric (TE)– and transverse magnetic (TM)–polarized incident light. As illustrated in Fig. 5H, all of the samples of 1D metallic nanostructures exhibited similar spectral reflectance of the polarized incident light (fig. S18). However, we observed that the highest contrast between TE and TM polarization corresponds to the 1D array of gold nanowires obtained from the quality-controlled 1D self-assembly pattern via optimized SS annealing. In addition, the spectral response is closest to the theoretical spectral responses of the 1D array of gold nanowires calculated by rigorous coupled wave approximation (RCWA) (*47*). Deviations of the experimental data from the RCWA calculations in UV-blue spectrum (i.e., 350 to 420 nm) may be attributed to the intrinsic plasmonic effects of the metallic nanostructures such as Fabry-Perot resonance along the longitudinal direction of the nanowires (*48*–*50*) or localized surface plasmonic resonance

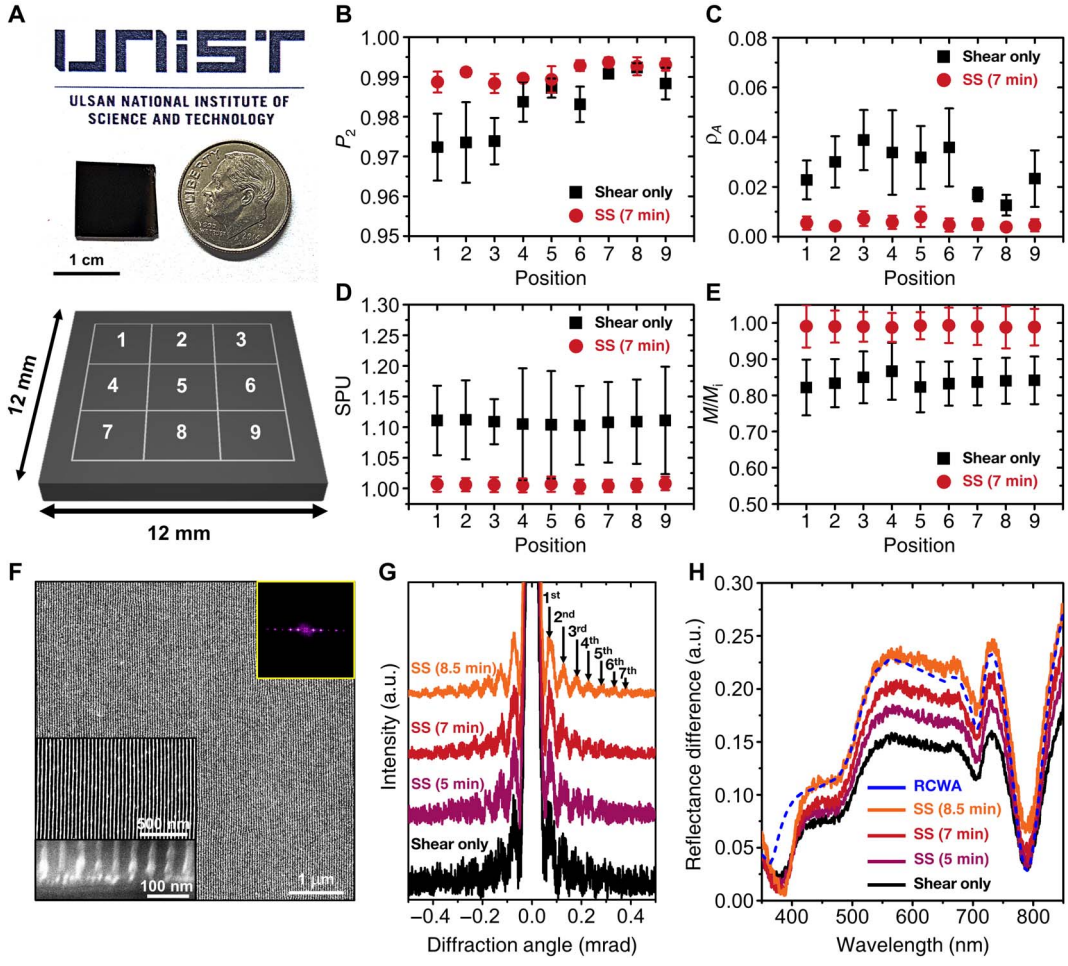

Fig. 5. Investigation of global uniformity of pattern quality in a large area. (**A**) Real image of a BCP thin film (1.2 cm by 1.2 cm) and a scheme showing nine-divided regions. (**B**) Hermans parameter, P_2, (**C**) areal defect density (ρ_A), (**D**) SPU, and (**E**) scaled magnitude after Gabor filtering (M/M_i) obtained from each of the nine regions. (**F**) SEM image of fabricated Au 1D array after SS annealing with mixture for 7 min. Left bottom insets show enlarged and tilted view SEM image of Au 1D array. The right top inset shows the FFT image obtained from the SEM image. (**G**) Semilog plots for the rocking curves of Au nanowires [shear-only and SS annealing with different times (5, 7, and 8.5 min)] obtained by x-ray double crystal Bragg diffraction. For the sample with SS for 8.5 min, we marked several peaks corresponding to sequential diffraction order with arrows. (**H**) Ultraviolet–visible–near-infrared spectrometral behaviors of Au nanowires [shear-only and SS annealing with different times (5, 7, and 8.5 min)]. The behaviors were obtained from reflectance difference between transverse electric– and transverse magnetic–polarized incident light from the sample. The blue dashed line indicates $R_{TE} - R_{TM}$ of 1D infinite parallel nanolines of Au on Si substrate calculated by rigorous coupled wave approximation.

(*51*). The observations based on the spectral responses to the polarized incident light also suggest that the centimeter-scale 1D metallic nanostructures exhibit promising features for fabrication of a high-performance wire-grid polarizer (*24*). On the basis of XRBD and spectral reflectance data, we conclude that SS annealing with optimized solvent selection and annealing time successfully resulted in nearly defect-free and nearly perfectly aligned BCP nanopatterns over a large area.

DISCUSSION

In conclusion, we demonstrated an experimental strategy for the fabrication of defect-annihilated BCP nanopatterns with a nearly perfect alignment and orientational order over a large area. We found that the combination of initial mechanical shearing and solvent unnecessary expression annealing under controlled annealing time, temperature, and solvent mixing ratios is essential to generate nearly defect-free self-assembled BCP nanopatterns sustaining orientational order. The performance of SS annealing was thoroughly analyzed and confirmed by measuring quantitative indices such as orientational order parameter, defect number and areal density, and SPU. Using coarse-grained computer simulations combined with an advanced sampling method, we also found that the defect annihilation was also induced by reducing the kinetic energy barrier, resulting from the controlled swelling of BCP nanopatterns incorporating optimized domain spacing. We thoroughly confirmed the superior performance of the SS annealing method developed by x-ray diffraction and the optical response of metallized BCP nanopatterns. In addition, the 1D array of metallic nanowires ensures application in other areas such as optoelectronic and photonic devices. The simplicity and robustness of the present annealing method can be easily extended to a wide range of BCP thin films, suggesting a substantial benefit based on quality-controlled BCP nanolithography and further applications based on bottom-up patterning.

MATERIALS AND METHODS

Sample preparation

PS-*b*-P2VP BCP with a number-average molecular weight of 44-*b*-18.5 kg/mol (dispersity Đ = 1.07) was purchased from Polymer Source Inc. and directly used without any further purification steps. Si wafers were purchased from Wafer Biz and spin-washed with fresh toluene before use. BCP solution (1.2 weight %) was prepared by dissolving in toluene, and spin-coating at 3000 rpm for 40 s led to creating ~38-nm-thick BCP thin films. The films thickness was measured using a spectroscopic ellipsometer (J.A. Woollam Co., M-2000V).

SS annealing

Sequential processing steps combining shear alignment and SVA were performed after the spin-coating of BCPs without any further treatments. First, shear alignment was performed by applying shear stress with a cured PDMS pad above T_g, as described in our previous works (*26*, *32*). The PDMS pads were prepared with SYLGARD 184 kit at a 10:1 ratio of PDMS elastomer base/curing agent mixture. The subsequent SVA was performed by placing shear-aligned BCP thin films in a glass chamber at room temperature; samples were placed in a 50-ml glass jar with the addition of 5 ml of desired solvent and sealed with a chamber lid. After the SVA process, samples were taken out of the glass chamber and blown with N_2 gas.

In situ swelling experiments

In situ observation of swelling ratio of polymer thin films was performed using a temperature-controlled custom-made chamber mounted on the ellipsometry, as described in the Supplementary Materials. After PS, P2VP, and PS-*b*-P2VP thin films were placed in the chamber, thickness variation was monitored at constant time intervals of 30 s. The surface-to-volume ratio of exposed solvent is 0.09 to 0.12 cm^{-1}.

SEM imaging

SEM (Hitachi S-4800) was used to characterize the morphologies of BCP thin films. The operation energy was 5 keV, and the working distance was 3 mm. Before imaging by SEM, gold loading on P2VP domain (*45*) was carried out for enhancing contrast by soaking the samples in a 5 mM $HAuCl_4$/3% HCl solution for 30 min. Subsequent rinsing with deionized water and blown with N_2 gas was conducted.

GISAXS measurements

GISAXS measurements were performed at the 6D UNIST-PAL beamline at the Pohang Accelerator Laboratory. The energy of the x-rays was 9.9 keV (wavelength, λ = 1.2523 Å), and the sample-to-detector distance was 3512.4 mm. 2D data were collected with a 2D charge-coupled device detector (MX225-HS, Rayonix LLC, USA). Before the measurements, gold loading on P2VP cylinders was performed to enhance the electron density contrast. All measurements were performed with the incident beam parallel to the alignment direction.

Model and methods

Advanced rare-event sampling technique named as the string method was used to investigate the kinetic energy variation during the defect annihilation in BCP thin films, in combination with the TICG model. The TICG model takes advantage of having explicit polymer chains expressed with Gaussian bead spring model, while nonbonded Hamiltonian is evaluated based on polymeric field theoretic form: $H_{nb} = \frac{\rho_0 k_B T}{N}\int_V dr\left(\chi N\phi_A(r)\phi_B(r) + \frac{\kappa N}{2}(\phi_A(r) + \phi_B(r) - 1)^2\right)$, where $\phi_\alpha = \frac{\rho_\alpha}{\rho_0}$ denotes the normalized number density of species α and ρ_0, χ, and κ are the average bulk number density of beads, Flory parameter, and the inverse compressibility, respectively. A string connecting defective and defect-free structures with a contour variable (reaction coordinate α) varying from 0 and 1 was defined on a multidimensional collective variable (CV) space constructed with density fields on a spatial grid over the simulation box. Each component of CV **m** is defined by normalized order parameter $\frac{\phi_A(r_i)-\phi_B(r_i)}{\phi_A(r_i)+\phi_B(r_i)}$, where $\phi_A(r_i)$ and $\phi_B(r_i)$ are density values of A and B segments at the grid of r_i. Among many possible strings connecting two states, the MFEP was defined with a string along which the gradient of free energy disappears. At each iteration of updating the string, a free energy gradient at 128 nodes uniformly distributed along the string was evaluated by umbrella sampling restraining TICG Monte Carlo simulations to be around corresponding CV **m** by adding the additional potential, $H_c(r^{nN} \mid \mathbf{m}) = \frac{\lambda k_B T}{2}\Delta L^3[\mathbf{m} - \hat{\mathbf{m}}]^2$. $\hat{\mathbf{m}}$ is the CV value for particle coordinates, r^{nN}. Then, the free energy gradient can be estimated by $\lambda\Delta L^3 k_B T[\mathbf{m} - \langle\hat{\mathbf{m}}\rangle_c] \xrightarrow{\lambda\to\infty} \frac{\mathcal{F}}{\partial\mathbf{m}}$. The string was updated using Euler technique, $\mathbf{m}|^1 = \mathbf{m}|^0 - \tau\lambda[\mathbf{m}|^0 - \langle\hat{\mathbf{m}}\rangle_c]$, at every node. Once the string was converged, free energy values at every node were estimated from $\Delta\mathcal{F}[\alpha] = \int_0^\alpha ds \frac{\partial\mathcal{F}}{\partial\mathbf{m}}|_{\mathbf{m}(s)} \cdot \frac{d\mathbf{m}(s)}{ds}$. Our simulations were conducted for lamellar-forming symmetric BCP thin films, which is shown to have qualitatively similar defect annihilation behavior as cylinder-forming cases (*52*). Simulation box size in the lateral direction was chosen to be six times of various periodicity *L* (*d*-spacing) of 1.655, 1.728, 1.8, 1.9, 2.0, and 2.1R_e, end-to-end distance, while L_y and L_z (film thickness) were fixed at 8.275 and 1.655R_e, respectively. For our calculations, we used the values $\sqrt{N} = \frac{\rho_0 R_e^3}{N} = 128$, $\chi N = 20$, $\kappa N = 50$, and $\lambda = \frac{3000}{R_e^3}$. The step size for string update, τ, was chosen to vary depending on the systems from 0.025 to 0.08. While our calculation was conducted for lamellar structures, qualitative behavior of defect annihilation is expected to be similar to cylinder-forming cases (*52*).

Fabrication of Au nanowires array

To generate the 1D array of gold nanowires, the anions of Au precursors were first loaded on the P2VP cylindrical domains, as described in the "SEM imaging" section (immersing the films in 5 mM $HAuCl_4$/3% HCl solution for 30 min). After Au ion loading, an O_2 reactive ion etching process (60 W, 10 mtorr, and 10 sccm) was applied for 30 s to remove the PS domains and reduce the gold ions to solid gold structure (*32*). The unit of flow rate (sccm) represents standard cubic centimeters per minute.

X-ray double crystal Bragg diffraction

XRBD measurement was performed using a Bruker D8 X-ray double crystal diffractometer. The x-ray source was CuKα (λ = 0.154 nm) from a 6.5-kW copper target (50-kV rotation anode unit and vertical light source). The resolution of detector was 0.01 to 0.02 mrad, and the count rate was 40 to 60 counts per second.

UV-Vis-NIR–polarized reflectance measurements

UV-Vis-NIR spectral behavior was obtained using a PerkinElmer LAMBDA 950 two-beam spectrometer with a Cary 5000 detector (Agilent) with an integrating sphere. The incident light was introduced perpendicular to the substrate; the spectral region was 320 to 1080 nm, but data were only shown at the range of 350 to 850 nm because of the detector sensitivity.

RCWA calculation

RCWA calculation was done assuming 1D nanograting with reported dielectric constants of materials (Au, Si, and air). For the modeling of

the nanograting, we did not consider any remaining number of organic molecules from the BCP thin film. For the geometry of the 1D grating, we assumed a perfect rectangular cross-sectional shape with a height of 25 nm, a periodicity of 40 nm, and a width of 20 nm. For the numerical calculation, we modeled the 1D grating structure as an assembly of thin layers deposited along the normal direction of thin film. For each of the layers, we applied a scattering matrix algorithm, which automatically solves Maxwell equation considering boundary conditions. Detailed mathematical formulations and relevant solution algorithms can be found in literature (*47*).

SUPPLEMENTARY MATERIALS

Supplementary material for this article is available at http://advances.sciencemag.org/cgi/content/full/5/6/eaaw3974/DC1

Section S1. A temporal evolution of the structural order in SS-annealed BCP thin films
Section S2. Effects of initial shearing temperature for SS annealing on BCP thin films
Section S3. Analysis of peak broadening of a small-angle scattering peak as a function of fluctuations in the domain spacing and line width of 1D line-and-space patterns
Section S4. Calculation of the orientational order and correlation of self-assembled BCP thin films
Section S5. Detection and quantification of areal and number density of topological defects in self-assembled BCP thin films
Section S6. Calculation of the SPU of self-assembled patterns
Section S7. Gabor filtering and convolution for the measurement of the uniformity of self-assembled patterns in BCP thin films
Section S8. Measurement of the LER and LWR of self-assembled patterns
Section S9. Experimental details of SVA and swelling of BCP thin films
Section S10. Long-time SS annealing effects on the morphological stability and orientational order of BCP thin films
Section S11. Comparison of the domain spacing of BCP thin films with different film thicknesses under thermal annealing
Section S12. Effects of ST annealing on the self-assembled patterns in BCP thin films
Section S13. Comparison of morphological stability and structural order of BCP thin films annealed by different methods
Section S14. Large-area uniformity of self-assembled pattern of shear-only and SS-annealed BCP thin films
Section S15. UV-Vis-NIR reflectance of TE- and TM-polarized incident light from 1D metal nanowire array on the substrate
Fig. S1. A temporal evolution of the structural order in SS-annealed BCP thin films.
Fig. S2. Effects of initial shearing temperature and solvent vapor exposure time.
Fig. S3. Numerical calculation of broadening behavior of the primary scattering peak.
Fig. S4. Effects of the periodicity fluctuation of lamellae patterns on the small-angle scattering behavior.
Fig. S5. Procedure of orientation calculation and color mapping.
Fig. S6. Calculation of orientational correlation function, $g(r)$.
Fig. S7. Procedure for original raw SEM image to precisely detect topological defects and measure their areal densities in the self-assembled pattern of BCP thin films.
Fig. S8. Procedure for the calculation of number density of the topological defects in the BCP thin films using the fingerprint analysis algorithm.
Fig. S9. Calculation of SPU.
Fig. S10. A measurement of a line-and-space pattern uniformity using a Gabor filter.
Fig. S11. Measurement of the LER and LWR of self-assembled BCP thin films using a commercially available software (SuMMIT).
Fig. S12. Swelling experiments of BCP and homopolymer thin films.
Fig. S13. Effects of SS annealing on the film stability and pattern uniformity of BCP thin films after long-time exposure to solvent.
Fig. S14. Calculation of domain d-spacing of thermally annealed BCP thin films with different film thicknesses.
Fig. S15. Experimental results for the self-assembled pattern quality of BCP thin films after ST annealing.
Fig. S16. Effects of different combinations of annealing methods on the structural order and film stability of BCP thin films.
Fig. S17. Comparison of large-area uniformity of self-assembled patterns of shear-only and SS-annealed BCP thin films.
Fig. S18. UV-Vis-NIR reflectance spectra from a 1D parallelly aligned array of gold nanowires.
Table S1. An algorithm for the calculation of SPU.
Table S2. Comparison of optimized condition and long-time SS annealing.
References (*53*–*61*)

REFERENCES AND NOTES

1. B. H. Mun, B. K. You, S. R. Yang, H. G. Yoo, J. M. Kim, W. I. Park, Y. Yin, M. Byun, Y. S. Jung, K. J. Lee, Flexible one diode-one phase change memory array enabled by block copolymer self-assembly. *ACS Nano* **9**, 4120–4128 (2015).
2. J. Y. Kim, H. Kim, B. H. Kim, T. Chang, J. Lim, H. M. Jin, J. H. Mun, Y. J. Choi, K. Chung, J. Shin, S. Fan, S. O. Kim, Highly tunable refractive index visible-light metasurface from block copolymer self-assembly. *Nat. Commun.* **7**, 12911 (2016).
3. Y. Yang, H. Kim, J. Xu, M.-S. Hwang, D. Tian, K. Wang, L. Zhang, Y. Liao, H. G. Park, G.-R. Yi, X. Xie, J. Zhu, Responsive block copolymer photonic microspheres. *Adv. Mater.* **30**, 1707344 (2018).
4. D. O. Shin, J.-R. Jeong, T. H. Han, C. M. Koo, H.-J. Park, Y. T. Lim, S. O. Kim, A plasmonic biosensor array by block copolymer lithography. *J. Mater. Chem.* **20**, 7241–7247 (2010).
5. M. P. Stoykovich, P. F. Nealey, Block copolymers and conventional lithography. *Mater. Today* **9**, 20–29 (2006).
6. I. Bita, J. K. W. Yang, Y. S. Jung, C. A. Ross, E. L. Thomas, K. K. Berggren, Graphoepitaxy of self-assembled block copolymers on two-dimensional periodic patterned templates. *Science* **321**, 939–943 (2008).
7. Y. H. Hur, S. W. Song, J. M. Kim, W. I. Park, K. H. Kim, Y. J. Kim, Y. S. Jung, Thermodynamic and kinetic tuning of block copolymer based on random copolymerization for high-quality sub-6 nm pattern formation. *Adv. Funct. Mater.* **28**, 1800765 (2018).
8. S. O. Kim, H. H. Solak, M. P. Stoykovich, N. J. Ferrier, J. J. De Pablo, P. F. Nealey, Epitaxial self-assembly of block copolymers on lithographically defined nanopatterned substrates. *Nature* **424**, 411–414 (2003).
9. R. Ruiz, H. Kang, F. A. Detcheverry, E. Dobisz, D. S. Kercher, T. R. Albrecht, J. J. de Pablo, P. F. Nealey, Density multiplication and improved lithography by directed block copolymer assembly. *Science* **321**, 936–939 (2008).
10. H. M. Jin, S. H. Lee, J. Y. Kim, S. W. Son, B. H. Kim, H. K. Lee, J. H. Mun, S. K. Cha, J. S. Kim, P. F. Nealey, K. J. Lee, S. O. Kim, Laser writing block copolymer self-assembly on graphene light-absorbing layer. *ACS Nano* **10**, 3435–3442 (2016).
11. P. W. Majewski, K. G. Yager, Millisecond ordering of block copolymer films via photothermal gradients. *ACS Nano* **9**, 3896–3906 (2015).
12. M. Gopinadhan, Y. Choo, K. Kawabata, G. Kaufman, X. Feng, X. di, Y. Rokhlenko, L. H. Mahajan, D. Ndaya, R. M. Kasi, C. O. Osuji, Controlling orientational order in block copolymers using low-intensity magnetic fields. *Proc. Natl. Acad. Sci. U.S.A.* **114**, E9437–E9444 (2017).
13. H. U. Jeon, H. M. Jin, J. Y. Kim, S. K. Cha, J. H. Mun, K. E. Lee, J. J. Oh, T. Yun, J. S. Kim, S. O. Kim, Electric field directed self-assembly of block copolymers for rapid formation of large-area complex nanopatterns. *Mol. Syst. Des. Eng.* **2**, 560–566 (2017).
14. S.-J. Jeong, J. Y. Kim, B. H. Kim, H.-S. Moon, S. O. Kim, Directed self-assembly of block copolymers for next generation nanolithography. *Mater. Today* **16**, 468–476 (2013).
15. S.-M. Hur, V. Thapar, A. Ramírez-Hernández, G. Khaira, T. Segal-Peretz, P. A. Rincon-Delgadillo, W. Li, M. Müller, P. F. Nealey, J. J. de Pablo, Molecular pathways for defect annihilation in directed self-assembly. *Proc. Natl. Acad. Sci. U.S.A.* **112**, 14144–14149 (2015).
16. U. Nagpal, M. Müller, P. F. Nealey, J. J. de Pablo, Free energy of defects in ordered assemblies of block copolymer domains. *ACS Macro Lett.* **1**, 418–422 (2012).
17. H. Takahashi, N. Laachi, K. T. Delaney, S.-M. Hur, C. J. Weinheimer, D. Shykind, G. H. Fredrickson, Defectivity in laterally confined lamella-forming diblock copolymers: Thermodynamic and kinetic aspects. *Macromolecules* **45**, 6253–6265 (2012).
18. A. M. Welander, H. Kang, K. O. Stuen, H. H. Solak, M. Müller, J. J. de Pablo, P. F. Nealey, Rapid directed assembly of block copolymer films at elevated temperatures. *Macromolecules* **41**, 2759–2761 (2008).
19. S.-M. Hur, V. Thapar, A. Ramírez-Hernández, P. F. Nealey, J. J. de Pablo, Defect annihilation pathways in directed assembly of lamellar block copolymer thin films. *ACS Nano* **12**, 9974–9981 (2018).
20. H. M. Jin, D. Y. Park, S.-J. Jeong, G. Y. Lee, J. Y. Kim, J. H. Mun, S. K. Cha, J. Lim, J. S. Kim, K. H. Kim, K. J. Lee, S. O. Kim, Flash light millisecond self-assembly of high χ block copolymers for wafer-scale sub-10 nm nanopatterning. *Adv. Mater.* **29**, 1700595 (2017).
21. P. W. Majewski, K. G. Yager, Latent alignment in pathway-dependent ordering of block copolymer thin films. *Nano Lett.* **15**, 5221–5228 (2015).
22. B. H. Kim, S. J. Park, H. M. Jin, J. Y. Kim, S. W. Son, M. H. Kim, C. M. Koo, J. Shin, J. U. Kim, S. O. Kim, Anomalous rapid defect annihilation in self-assembled nanopatterns by defect melting. *Nano Lett.* **15**, 1190–1196 (2015).
23. D. E. Angelescu, J. H. Waller, D. H. Adamson, P. Deshpande, S. Y. Chou, R. A. Register, P. M. Chaikin, Macroscopic orientation of block copolymer cylinders in single-layer films by shearing. *Adv. Mater.* **16**, 1736–1740 (2004).
24. S. Y. Kim, J. Gwyther, I. Manners, P. M. Chaikin, R. A. Register, Metal-containing block copolymer thin films yield wire grid polarizers with high aspect ratio. *Adv. Mater.* **26**, 791–795 (2014).
25. S. Y. Kim, A. Nunns, J. Gwyther, R. L. Davis, I. Manners, P. M. Chaikin, R. A. Register, Large-area nanosquare arrays from shear-aligned block copolymer thin films. *Nano Lett.* **14**, 5698–5705 (2014).

26. Y. C. Kim, D. H. Kim, S. H. Joo, N. K. Kwon, T. J. Shin, R. A. Register, S. K. Kwak, S. Y. Kim, Log-rolling block copolymer cylinders. *Macromolecules* **50**, 3607–3616 (2017).
27. Z. Qiang, L. Zhang, G. E. Stein, K. A. Cavicchi, B. D. Vogt, Unidirectional alignment of block copolymer films induced by expansion of a permeable elastomer during solvent vapor annealing. *Macromolecules* **47**, 1109–1116 (2014).
28. G. Singh, K. G. Yager, B. Berry, H.-C. Kim, A. Karim, Dynamic thermal field-induced gradient soft-shear for highly oriented block copolymer thin films. *ACS Nano* **6**, 10335–10342 (2012).
29. J. Jeong, J. S. Ha, S. S. Lee, J. G. Son, Topcoat-assisted perpendicular and straightly parallel coexisting orientations of block copolymer films. *Macromol. Rapid Commun.* **36**, 1261–1266 (2015).
30. R. L. Davis, P. M. Chaikin, R. A. Register, Cylinder orientation and shear alignment in thin films of polystyrene–poly (*n*-hexyl methacrylate) diblock copolymers. *Macromolecules* **47**, 5277–5285 (2014).
31. A. P. Marencic, P. M. Chaikin, R. A. Register, Orientational order in cylinder-forming block copolymer thin films. *Phys. Rev. E* **86**, 021507 (2012).
32. Y. C. Kim, S. Y. Kim, Fabrication of gold nanowires in micropatterns using block copolymers. *RSC Adv.* **8**, 19532–19538 (2018).
33. J. H. Mun, S. K. Cha, Y. C. Kim, T. Yun, Y. J. Choi, H. M. Jin, J. E. Lee, H. U. Jeon, S. Y. Kim, S. O. Kim, Controlled segmentation of metal nanowire array by block copolymer lithography and reversible ion loading. *Small* **13**, 1603939 (2017).
34. S. Förster, A. Timmann, M. Konrad, C. Schellbach, A. Meyer, S. S. Funari, P. Mulvaney, R. Knott, Scattering curves of ordered mesoscopic materials. *J. Phys. Chem. B* **109**, 1347–1360 (2005).
35. X. Gu, I. Gunkel, A. Hexemer, W. Gu, T. P. Russell, An in situ grazing incidence x-ray scattering study of block copolymer thin films during solvent vapor annealing. *Adv. Mater.* **26**, 273–281 (2014).
36. I. Gunkel, X. Gu, Z. Sun, E. Schaible, A. Hexemer, T. P. Russell, An in situ GISAXS study of selective solvent vapor annealing in thin block copolymer films: Symmetry breaking of in-plane sphere order upon deswelling. *J. Polym. Sci. B* **54**, 331–338 (2016).
37. N. L. Wu, X. Zhang, J. N. Murphy, J. Chai, K. D. Harris, J. M. Buriak, Density doubling of block copolymer templated features. *Nano Lett.* **12**, 264–268 (2011).
38. W. I. Park, S. Tong, Y. Liu, I. W. Jung, A. Roelofs, S. Hong, Tunable and rapid self-assembly of block copolymers using mixed solvent vapors. *Nanoscale* **6**, 15216–15221 (2014).
39. Y. S. Jung, C. A. Ross, Solvent-vapor-induced tunability of self-assembled block copolymer patterns. *Adv. Mater.* **21**, 2540–2545 (2009).
40. C. T. Black, K. W. Guarini, Y. Zhang, H. Kim, J. Benedict, E. Sikorski, I. V. Babich, K. R. Milkove, High-capacity, self-assembled metal-oxide-semiconductor decoupling capacitors. *IEEE Electron Device Lett.* **25**, 622–624 (2004).
41. R. A. Griffiths, A. Williams, C. Oakland, J. Roberts, A. Vijayaraghavan, T. Thomson, Directed self-assembly of block copolymers for use in bit patterned media fabrication. *J. Phys. D Appl. Phys.* **46**, 503001 (2013).
42. J. H. Mun, Y. H. Chang, D. O. Shin, J. M. Yoon, D. S. Choi, K. M. Lee, J. Y. Kim, S. K. Cha, J. Y. Lee, J. R. Jeong, Y. H. Kim, S. O. Kim, Monodisperse pattern nanoalloying for synergistic intermetallic catalysis. *Nano Lett.* **13**, 5720–5726 (2013).
43. M. Fan, G. F. Andrade, A. G. Brolo, A review on the fabrication of substrates for surface enhanced Raman spectroscopy and their applications in analytical chemistry. *Anal. Chim. Acta* **693**, 7–25 (2011).
44. P. A. Mistark, S. Park, S. E. Yalcin, D. H. Lee, O. Yavuzcetin, M. T. Tuominen, T. P. Russell, M. Achermann, Block-copolymer-based plasmonic nanostructures. *ACS Nano* **3**, 3987–3992 (2009).
45. J. Chai, D. Wang, X. Fan, J. M. Buriak, Assembly of aligned linear metallic patterns on silicon. *Nat. Nanotechnol.* **2**, 500–506 (2007).
46. F. A. Jenkins, H. E. White, *Fundamentals of Optics* (McGraw-Hill, ed. 3, 1957).
47. M. Moharam, T. K. Gaylord, Rigorous coupled-wave analysis of planar-grating diffraction. *J. Opt. Soc. Am.* **71**, 811–818 (1981).
48. M. Aramesh, J. Cervenka, A. Roberts, A. Djalalian-Assl, R. Rajasekharan, J. Fang, K. Ostrikov, S. Prawer, Coupling of a single-photon emitter in nanodiamond to surface plasmons of a nanochannel-enclosed silver nanowire. *Opt. Express* **22**, 15530–15541 (2014).
49. J. Dorfmüller, R. Vogelgesang, W. Khunsin, C. Rockstuhl, C. Etrich, K. Kern, Plasmonic nanowire antennas: Experiment, simulation, and theory. *Nano Lett.* **10**, 3596–3603 (2010).
50. L. Piazza, T. T. A. Lummen, E. Quiñonez, Y. Murooka, B. W. Reed, B. Barwick, F. Carbone, Simultaneous observation of the quantization and the interference pattern of a plasmonic near-field. *Nat. Commun.* **6**, 6407 (2015).
51. L. Zhao, K. L. Kelly, G. C. Schatz, The extinction spectra of silver nanoparticle arrays: Influence of array structure on plasmon resonance wavelength and width. *J. Phys. Chem. B* **107**, 7343–7350 (2003).
52. B. Kim, N. Laachi, K. T. Delaney, M. Carilli, E. J. Kramer, G. H. Fredrickson, Thermodynamic and kinetic aspects of defectivity in directed self-assembly of cylinder-forming diblock copolymers in laterally confining thin channels. *J. Appl. Polym. Sci.* **131**, 40790 (2014).
53. B. Crist, J. Cohen, Fourier analysis of polymer x-ray diffraction patterns. *J. Polym. Sci. B* **17**, 1001–1010 (1979).
54. X. Feng, P. Milanfar, *Conference Record of the Thirty-Sixth Asilomar Conference on Signals, Systems and Computers, 2002* (IEEE, 2002), vol. 1, pp. 478–482.
55. M. Ullner, C. E. Woodward, Orientational correlation function and persistence lengths of flexible polyelectrolytes. *Macromolecules* **35**, 1437–1445 (2002).
56. J. N. Murphy, K. D. Harris, J. M. Buriak, Automated defect and correlation length analysis of block copolymer thin film nanopatterns. *PLOS ONE* **10**, e0133088 (2015).
57. M. J. Hytch, Analysis of variations in structure from high resolution electron microscope images by combining real space and Fourier space information. *Microsc. Microanal. Microstruct.* **8**, 41–57 (1997).
58. M. Seyring, X. Song, A. Chuvilin, U. Kaiser, M. Rettenmayr, Characterization of grain structure in nanocrystalline gadolinium by high-resolution transmission electron microscopy. *J. Mater. Res.* **24**, 342–346 (2009).
59. C. Tomasi, R. Manduchi, in *Sixth International Conference on Computer Vision, 1998* (IEEE, 1998), pp. 839–846.
60. S. A. Sudiro, M. Paindavoine, T. M. Kusuma, in *2007 IEEE Workshop on Automatic Identification Advanced Technologies* (IEEE, 2007), pp. 41–44.
61. M. Haghighat, S. Zonouz, M. Abdel-Mottaleb, in *International Conference on Computer Analysis of Images and Patterns* (Springer, 2013), pp. 440–448.

Acknowledgments: GISAXS experiments at PLS-II 6D beamline of the Pohang Accelerator Laboratory were supported in part by UCRF, MSIP, and POSTECH. We also thank J. G. Son at KIST for helpful communications. **Funding:** This work was supported through the National Research Foundation of Korea (NRF) funded by the Ministry of Education (2018R1A2B6008319, 2018R1A5A1024127, and 2017R1A2B3006469). This work was also supported by NRF-2018R1A5A 1025224 and the institutional research program of KIST (2E28070). **Author contributions:** S.Y.K. initiated and supervised the project. Y.C.K. principally performed experiments. S.Y.K., S.J.K., and S.-M.H. coordinated the research. T.J.S. helped with the GISAXS experiments. S.-M.H. performed molecular simulations. S.J.K. developed a set of numerical algorithms to treat raw data obtained from SEM images. S.J.K. calculated the 2D map of the orientational angle, orientational order parameter, orientational order correlation function, and orientational order correlation length. S.J.K. calculated number density and areal defect density. S.J.K. experimentally measured XRBD and UV-Vis-NIR spectral behaviors. All authors contributed to the manuscript preparation. **Competing interests:** The authors declare that they have no competing interests. **Data and materials availability:** All data needed to evaluate the conclusions in the paper are present in the paper and/or the Supplementary Materials. Additional data related to this paper may be requested from the authors.

Submitted 17 December 2018
Accepted 3 May 2019
Published 14 June 2019
10.1126/sciadv.aaw3974

Citation: Y. C. Kim, T. J. Shin, S.-M. Hur, S. J. Kwon, S. Y. Kim, Shear-solvo defect annihilation of diblock copolymer thin films over a large area. *Sci. Adv.* **5**, eaaw3974 (2019).

ScienceAdvances

Shear-solvo defect annihilation of diblock copolymer thin films over a large area

Ye Chan Kim, Tae Joo Shin, Su-Mi Hur, Seok Joon Kwon and So Youn Kim

Sci Adv **5** (6), eaaw3974.
DOI: 10.1126/sciadv.aaw3974